CORROSION PERFORMANCE OF NICKEL BASED ALLOY IN HYDROGEN IODINE SOLUTION

A Thesis

presented to

the Faculty of the Graduate School

at the University of Missouri-Columbia

In Partial Fulfillment

of the Requirements for the Degree

Master of Science

---

by

Muzhen Li

Dr. Patrick Pinhero, Thesis Supervisor

December 2016

The undersigned, appointed by the dean of the Graduate School, have examined the thesis entitled

CORROSION PERFORMANCE OF NICKEL BASED ALLOYS IN HYDROGEN IODINE SOLUTION

Presented by Muzhen Li,

a candidate for the degree of master of Science,

and hereby certify that, in their opinion, it is worthy of acceptance.

Professor Patrick Pinhero

Professor Qingsong Yu

Professor Bret Ulery

ACKNOWLEDGEMENTS

First and foremost, I would like to express my sincere gratitude to Dr. Pinhero for the valuable guidance and advice. He inspired me greatly to work in my research. His willingness to motivate me contributed tremendously to my research project.

I would also like to thank Dr. Qingsong Yu and Dr. Bret Ulery for their willingness to be members of my thesis committee and for offering me with kind help to complete this research program.

In addition, I would like to thank all the members of Dr. Patrick Pinhero's research group for their help and encouragement, especially Shendu Yang and Zach Thacker, who gave me lots of helpful suggestions. Finally, an honorable mention goes to my parents and friends for their supports and help on us in completing this research program.

TABLE OF CONTENTS

LIST OF FIGURES

LIST OF ABBREVIATIONS

Hydrogen Iodide	HI
Scanning electron microscopy	SEM
Sulfur-iodine thermochemical cycle process	S-I
Deionized water	DI water
X-ray energy dispersive spectroscopy	EDS
Electrochemical impedance spectroscopy	EIS
Cyclic Voltammetry	CV

ABSTRACT

In this thesis, the corrosion performance of some Ni-based super alloys including Inconel 625, Hastelloy X and Nickel 200 were investigated in HI solution at 70℃and 100℃ at intervals of 24h, 48h, 96h and 192h respectively. Morphology and microstructure of corroded samples were analyzed using scanning electron microscopy (SEM), X-ray energy dispersive spectroscopy (EDS), and optical profilometry. Corroded samples were also examined for their electrochemical corrosion properties by a cyclic voltammetry (CV) and electrochemical impedance spectroscopy (EIS).

The corrosion rates of all tested alloys increase with temperature. For Inconel 625 and Hastelloy X, the corrosion rate initially increased and then remained constant over time. This phenomenon is most probably attributable to their inherent anti-corrosion oxide layer. However, the corrosion rate for Nickel 200 does not fluctuate remarkably, since the protective layer is weaker than the other two alloys. In Inconel 625 samples, the constituent iron is lost in a stable ratio of rates with respect to nickel. While in Hastelloy X samples, the iron, Chromium, and Molybdenum are corroded in a stable ratio of rates with respect to nickel, respectively. With temperature increase, the corrosion rates of these elements increase.

The protective oxide layer of Hastelloy X is more anti-corrosive than Inconel 625, according to EIS results. And Hastelloy X has a smoother surface after several days' corrosion as observed by optical profilometry.

Keyword: Corrosion; Nickel-based alloy; Hydrogen Iodine; electrochemical property

CHAPTER 1

INTRODUCTION

Hydrogen is an effective and clean fuel. Thermochemical cycles are considered as acceptable methods to produce hydrogen on large scale. One of the most promising thermochemical cycles for hydrogen production is the Sulfur-Iodide (S-I) Cycle(Gorensek 2010) using nuclear energy. One of the important reagents within the S-I cycle is hydrogen iodide (or iodic acid), which is generally recognized as a highly-corrosive compound. Nickel-Chromium based alloys are famous for their high corrosion resistance. Therefore, the study of the corrosion of Nickel-based alloys in hydrogen iodide solutions is necessary for evaluating their application in future S-I hydrogen production process plants.

1.1 Introduction of Sulfur-Iodine Cycle

Increasing energy consumption, high cost, and limited amount of fossil fuels have spurred interest in the investigation of an economically profitable and high-conversion rate method for large-scale hydrogen production. One potential hydrogen-production process family that meets this requirement is thermochemical cycles. In thermochemical water-splitting cycles, cyclic chemical reactions are utilized where water reacts with chemical reagents. The products of these chemical reactions can then be thermally decomposed to yield hydrogen and oxygen at lower temperatures when compared to direct thermal decomposition of water (Nguyen, Gho et al. 2014). Therefore, water is considered as the only feedstock for this kind of processes. There are several

thermochemical cycle methods to product hydrogen, for example, UT-3 cycle(Lee, Goswami et al. 2009), Westinghouse hybrid cycle(Jomard, Feraud et al. 2008) and the aforementioned sulfur-iodine (S-I) cycle. Amon(Barbosa 2013)g these cycles, the S-I cycle proposed by General Atomics, is considered as a promising process for hydrogen production, due to its high efficiency (> 50%).

The S-I cycle consists of three coupled chemical reactions:

$$I_2 + SO_2 + 2H_2O \rightarrow 2HI + H_2SO_4 \qquad (70\text{-}120\ ℃)$$

$$H_2SO_4 \rightarrow SO_2 + H_2O + 0.5O_2 \qquad (>640℃)$$

$$2HI \rightarrow I_2 + H_2 \qquad (350\text{-}450\ ℃)$$

The S-I process flow is shown in Fig.1. In the first step, known as Bunsen reaction, iodine and sulfur dioxide are added into water, forming hydrogen iodide and sulfuric acid in the liquid phase(Ying, Zhang et al. 2013). In the left side of the figure, concentrated sulfuric acid decomposes between 800-900℃, liberating oxygen. The remaining sulfur dioxide is recycled in this cycle of the process. In the third reaction, shown on the right side of the figure, hydrogen iodide decomposes at temperatures greater than 350℃, releasing hydrogen and recycling iodine from the cycle as reactants for the next cycle(Murphy and O'Connell 2012). It has the advantage of being a purely thermochemical cycle, which requires virtually no electricity, thus avoiding the losses associated with the heat to electricity conversion. Furthermore, its coupling to the heat available from a generation VHTR nuclear reactor appears to be very attractive. Therefore,

the efficiency of this cycle is potentially high, and the associated hydrogen production costs potentially low, compared with the other thermochemical cycles.(Vitart, Le Duigou et al. 2006)

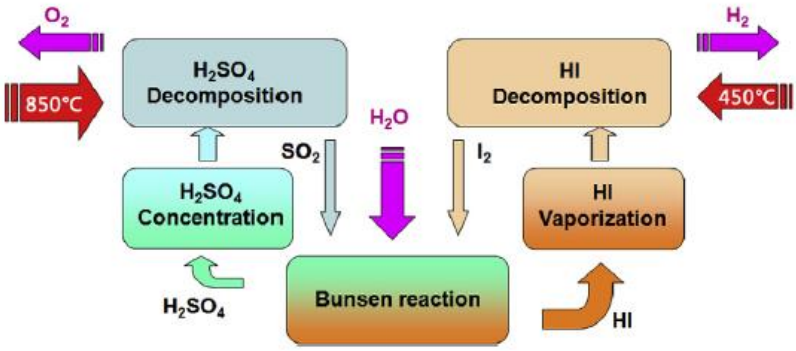

Figure 1 S-I thermochemical cycle for hydrogen production(Fu, Wang et al. 2016)

However, since the S-I thermochemical cycle reaction needs high temperature, high pressure and forms strong acid, this cycle also has number of technical issues associated with (Choi, Kim et al. 2014) its component materials of construction, which includes both prevention of material corrosion and selection of an appropriate catalyst. To mitigate the material corrosion issues, one could specify a highly-corrosion resistant material, such as nickel-based alloy.

1.2 Introduction of Nickel-based Alloys

Nickel-based alloys are widely used resist extreme conditions in the energy, power, chemical, and petrochemical industrial fields because of their near-perfect corrosion resistance(Brown, King et al. 2013). Many of these alloys are metallurgically-related to austenitic stainless steels but are much more highly-alloyed. For

Nickel-based alloys, besides the main element Ni, other elements, such as Cr, Mo, Mn are added to optimize the performance of the alloy according to different service environments (Liu, Zheng et al. 2013). In general, Cr is integrated to increase the corrosion resistance in oxidizing media; while Mo is used to enhance the strength and the anti-corrosive performance in reducing media (Liu, Zheng et al. 2013). Though more expensive than iron-based alloys, high-strength and high-corrosion-resistant nickel-based alloys are the favored practical material for hostile environments in many high-value applications where their optimum combination of heat and corrosion resistance often makes them the most economical long-term choice(Ross 2013).

In this study, we selected three different grades of Nickel alloys: Inconel 625, Hastelloy X, and Nickel 200. The component is shown in Table 1. Inconel 625 is a grade of nickel – chromium – molybdenum alloy with an addition of niobium that acts to stiffen the alloy's matrix and thereby provide higher strength without need of an additional heat treatment(Poza, Múnez et al. 2014). This alloy resists a wide range of severely corrosive environments and is especially resistant to pitting and crevice corrosion. It is used widely in chemical processing, aerospace, marine engineering and nuclear reactors. Hastelloy X is a grade of nickel – chromium – iron – molybdenum alloy with excellent heat and oxidation resistance; it also has good resistance to chloride stress-corrosion cracking and has good resistance to carburization(Wang 2012). It is one of the most widely used nickel base super alloy for gas turbine engine components. Nickel 200 is a kind of commercially pure wrought nickel with good mechanical properties and resistance to a range of corrosive media. It is used for a variety of

processing equipment, particularly to maintain product purity in handling foods, synthetic fibers.(Sitek, Krajewski et al. 2012) Usually, the unit price of Hastelloy X is the most expensive in these three alloys, while the unit price of Inconel 625 is just slightly cheaper. The unit cost of Nickel 200 is lowest.

Table 1 nominal compositions (wt. %) of the alloys provided by the manufacturers.

Element	Inconel 625	Hastelloy X	Nickel 200
Nickle(balance)	58.0 min	47.0	99.0 min
Chromium	20.0-23.0	22	
Iron	5.0 max	18	0.40max
Molybdenum	8.0 – 10.0	8.0-10.0	
Niobium	3.15-4.15		
Cobalt	1.0 max	1.5	
Silicon	0.5 max	1.0 max	0.35max
Aluminum	0.40 max	0.5 max	
Titanium	0.40 max	0.15 max	
Manganese	0.50max	1.0 max	0.35max

1.3 Aqueous Corrosion of Nickel Alloy

In aqueous corrosion processes, an interfacial electrochemical reaction occurs between the material and its service environment. In the S-I thermochemical process, it was discussed that one service environment is a HI water solution. Corrosion in this medium results in the material of interest being oxidized and HI being reduced. The redox process forms an electrochemical redox couple(Iden and Kucernak 2014). In the corrosion research discussed within this thesis, the corrosion of a Nickel alloy involves the coupling of the following two reactions:

Anodic: $\text{Metal} \rightarrow \text{Metal}^{2+} + 2e^-$

Cathodic: $2\,H^+ + 2e^- \rightarrow H_2$

The tendency for the reaction to proceed is given by the molar Gibbs free energy change (ΔG_{rxn}):

$$\Delta G_{rxn} = \sum \upsilon_p \mu_p + \sum \upsilon_r \mu_r$$

Where μ_p and μ_r are the product and reactant chemical potentials, respectively, and $\upsilon_p$and υ_r are their corresponding stoichiometric coefficients. The chemical potential, μ, of a substance is defined as:

$$\mu = \mu^0 + RTln\alpha$$

Where R is the universal gas constant, $8.314 JK^{-1}mol^{-1}$, T is the temperature, μ^0 is the standard chemical potential of the species, and α is the activity of the species. The Gibbs free energy of an electrochemical reaction at equilibrium can be defined as:

$$\Delta G_{rxn} = \ -nF\Delta E$$

Where n is the number of moles of electrons exchanged in the reaction, and F is the Faraday's constant (96,485 C mol^{-1})(Brookins 2012) and ΔE is the potential difference between the electrodes carrying the anodic and cathodic reactions, $\Delta E = E_{red} - E_{ox}$.

For dissolution of a metal species, the equilibrium potential is:

$$(E_e)_{M^{n+}/M} = (E^0)_{M^{n+}/M} - \frac{RT}{nF} ln a_{M^{n+}}$$

And for cathodic process, the equilibrium potential is:

$$(E_e)_{OX/Red} = (E^0)_{OX/Red} - \frac{RT}{nF} ln \frac{a_{red}}{a_{ox}}$$

Where E^0 is the standard potential for the half reaction, and a is the activity of the species(Vetter 2013).

1.4 Research Objective

The objective of this research is to study the corrosion performance of three nickel-based alloys in a set of HI service environments, differentiated by temperature and time of exposure. Since the corrosion process is an electrochemical process in nature, we decide to research the corrosion performance by electrochemical method in HI solution. The temperatures, 70℃ and 100℃, were chosen, to avoid the solution boiling under standard atmosphere pressure. We choose two compositions of Nickel-based alloy, Inconel 625 and Hastelloy X, to research the corrosion performance. At the same time, we also used Nickel 200 primarily as a pure Ni control, to demonstrate the functions of the other elements of controlling corrosion resistance in each of the two alloys. Some conventional analytical methods such as weight loss measurement, scanning electron

microscope (SEM) were employed to help resolve corrosive effects. Electrochemical methods, such as EIS and CV(Qiu, Tang et al. 2013), we utilized to quantify the corrosion behavior in HI solution.

The discussion of the corrosion mechanism will lead to a much more thorough understanding of nickel alloy corrosion, which is important for future application in hydrogen production by the thermochemical S-I process.

CHAPTER 2

EXPERIMENTAL PROCEDURES AND MATERIALS

2.1 Materials

Nickel alloy sheets (1.6mm * 1.5cm * 7.7cm) were purchased from High Performance Alloys, Inc. USA. HI solution (57 wt. % in H_2O, 99.99%) was purchased from Sigma-Aldrich. All experiments were completed using DI water.

2.2 Corrosion of Nickel Alloy

Three different grades of nickel alloy (Nickel 200, Hastelloy X, Inconel 625) sheet samples were ultrasonically-cleaned in acetone to remove organic contaminants, and rinsed with DI water. After drying with a nitrogen airflow, each sample was corroded in 250 ml de-aerated HI solution (29 wt. %) in a 500 ml flask under a nitrogen atmosphere and a controlled temperature, 70 ℃ and 100 ℃, for time intervals of 24 h, 48 h, 96 h and 192 h, respectively. The solution was refreshed with 250 ml of HI (29 wt.%) solution every 24 hour to complement the reacted HI. After corrosion, each sample was rinsed with DI water, dried with a nitrogen airflow, and then massed and evaluated.

2.3 Weight Loss Measurement

Before each corrosion experiment, and after the initial cleaning and drying procedure, each sample was massed and this original mass was recorded as m_{orig}. After

corrosion, each sample was cleaned and dried, and then was massed again. The final mass was recorded as m_{after}.

$$\text{Weight loss\%} = \frac{m_{orig} - m_{after}}{m_{orig}}$$

2.4 Surface Roughness Measurement

Optical profilometry measures surface topography from nanometer-scale roughness through millimeter-scale steps. This system also provides precise 3D surface metrology. The surface average roughness of each sample was measured using a Veeco WYKO NT 9109 optical profilometer.

2.5 Scanning Electron Microscopy

Each corroded sample was imaged using an FEI Quanta 600 Environmental Scanning Electron Microscope (ESEM; Hillsboro, OR). This scanning electron microscope (SEM) has useful capabilities for analyzing surfaces. The ESEM can operate in both high-vacuum and low-vacuum modes. It can operate with pressures around the sample up to 4000 Pa. A resolution of 1.5 nm can be detected and it has an accelerating voltage ranging from 0.5 to 30 kV. The elemental composition of each sample was determined employing Energy Dispersive Spectroscopy (EDS) attached to the ESEM(Goldstein, Newbury et al. 2012).

2.7 Cyclic Voltammetry (CV)

The CV analysis was performed by means of an computer-controlled potentiostat in 29 wt. % HI solution. The scan rate of CV was maintained at 20 mV/s. All experiments were carried out in a three-neck tempered quartz flask. An Ag/AgCl electrode was used as the reference electrode and a platinum sheet with an exposed area of 1 cm^2 was used as the counter electrode. The scan range is from 0 – 0.6 mV vs. E_{ref}. The pitting potential and repassivation potential were obtained from the CV plot.

2.8 Electrochemical impedance spectroscopy (EIS)

The EIS corrosion analysis was conducted using a potentiostat and performed in a 100 ml three-neck flask. A platinum sheet was used as the counter electrode, and an Ag/AgCl electrode was used as the reference electrode. The area of working electrode was controlled as 0.25cm^2. All electrochemical experiments were performed in 29 wt. % HI solution. Spectra were acquired at open circuit potential with a perturbing signal of 10 mV. The frequency span generally ranged from 100 kHz to 0.1Hz. Data fitting was performed using Gamry Data Analysis software with a nonlinear least- squares method.

Chapter 3

Results and Discussion

In this chapter, we analyze the results of weight loss and surface roughness obtained from the corrosion of the three grades of nickel alloys. The characterizations of morphology are also presented in order to provide a general understanding of the corrosion process. Data from the CV experiments and EIS are used to attempt to help quantify the corrosion performance more thoroughly.

3.1 Weight Loss Measurement

A simple way to observe corrosion performance is to perform weight loss measurements. Here we measure the three grades of Ni-based alloys in 29wt. % HI solution for various time periods and two temperatures. Figure 2 and Figure 3 show the tendency of the weight loss data of samples. Weight loss of all samples increases with temperature increases. This follows simple intuition because as the temperature rises, the rate of ion diffusion also goes up, which will lead to an increasing corrosion rate. In the first 24 hours, Inconel 625 specimens lost more mass than Hastelloy X specimens, but over the course of the next few days, Hastelloy X specimens lost more mass than Inconel 625. The protective layer, which we usually consider to be Cr_2O_3 with a mixture of other component metallic oxides in Inconel 625 samples, is not as anti-corrosive as Hastelloy X, while the internal composition of Inconel 625 has better resistance of corrosion.(Mishra and Shoesmith 2015)

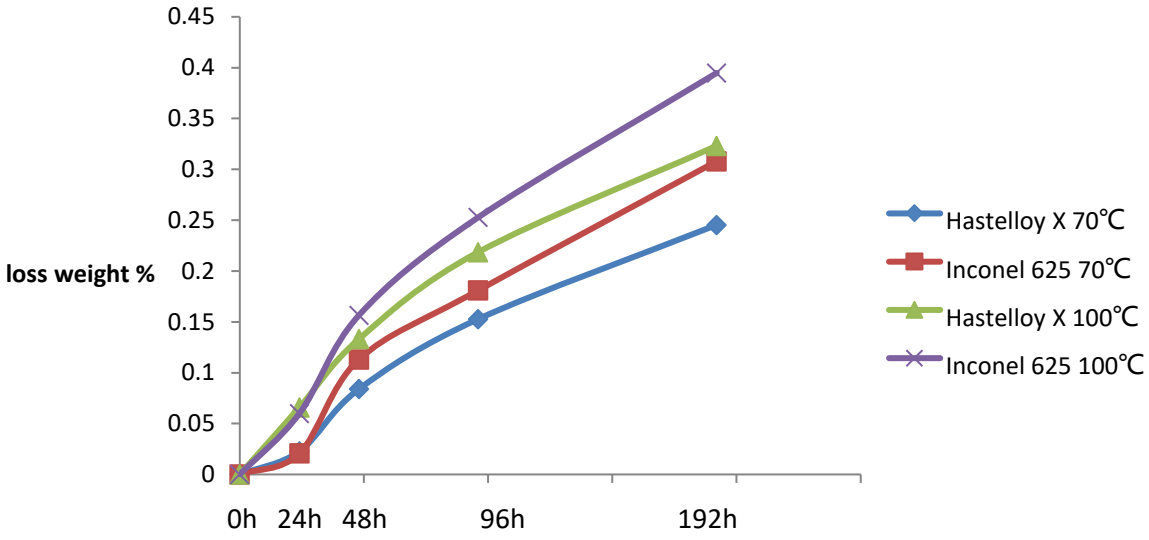

Figure 2 weight loss of Inconel 625 and Hastelloy X

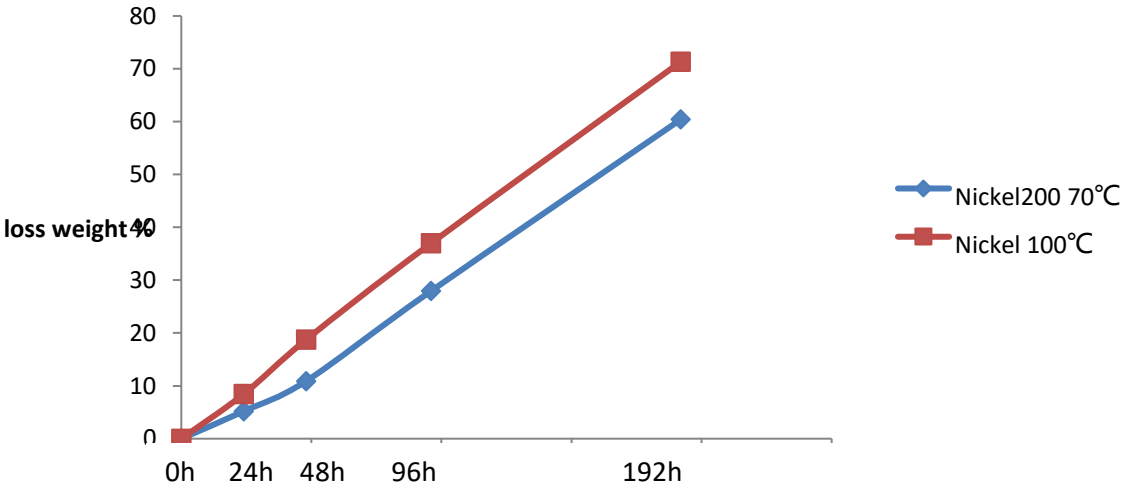

Figure 3 weight loss of Nickel 200

Figure 4 and Figure 5 indicate the rate of corrosion of three samples in different period.

$$\text{Rate of corrosion} = \frac{\partial \ loss \ \ weight(wt.\%)}{\partial \ \ \tau}$$

All of the rates of corrosion of samples go up when time increases, and get a maximum rate of corrosion between the 24 - 48 hours, then returns to a relatively stable rate. The

final corrosion rate of Inconel 625 is lower than Hastelloy X according to Fig 4. The good resistance of the protective layer leads to a low rate of corrosion in the first 24 hours of the corrosion experiment, but when the protective layer began to corrode, the rate of corrosion increases until the protective layer is corroded completely. It is then that the rate of corrosion decreases and goes flat since it is inhibited by the corrosion resistance of internal structure of the alloy. The corrosion rates of Nickel 200 samples are relatively similar, since the protective layer of Nickel 200 samples is not as anti-corrosive compared with the other two alloys. In the first 24 hours, the protective layer is almost completely corroded.

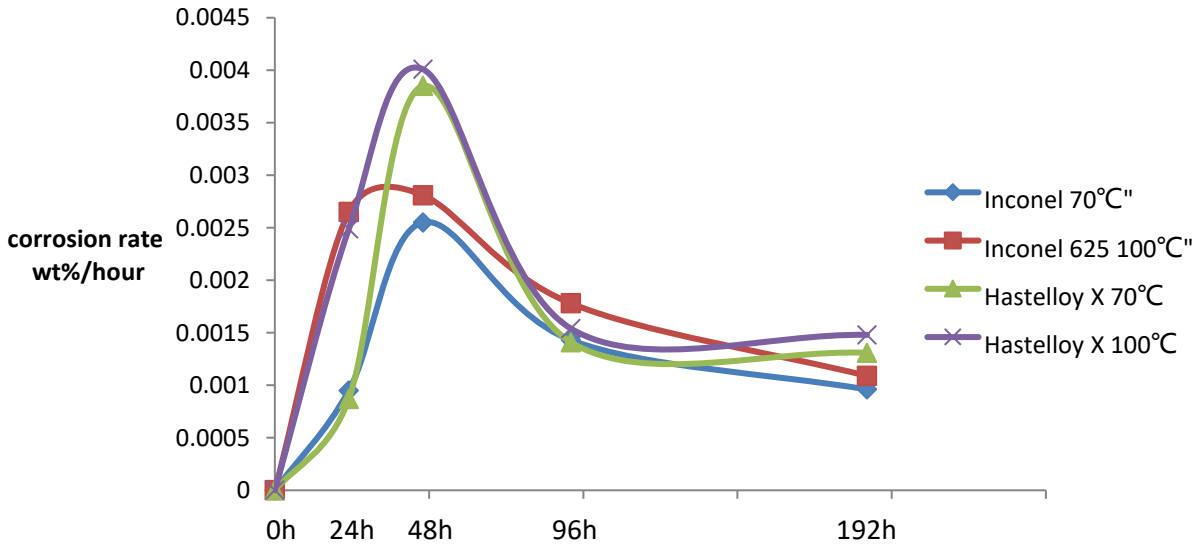

Figure 4 corrosion rate wt. % / hour of Inconel 625 and Hastelloy X

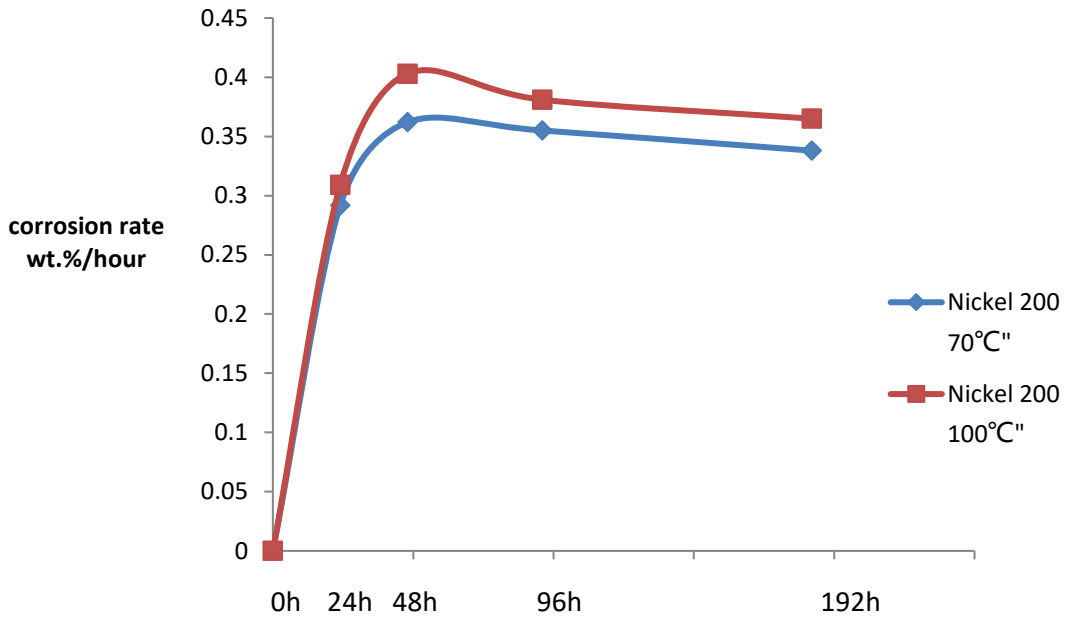

Figure 5 corrosion rate wt. % / hour of Nickel 200

3.2 Surface Morphology Analysis

As the time intervals increase and the temperature increases, the average roughness of all three alloy samples surface rises up according to Fig 6, Fig 7 and Fig 8. Fig 9 shows that for the same temperature and after same time corrosion, the average roughness of Hastelloy X sample is lower than Inconel 625.

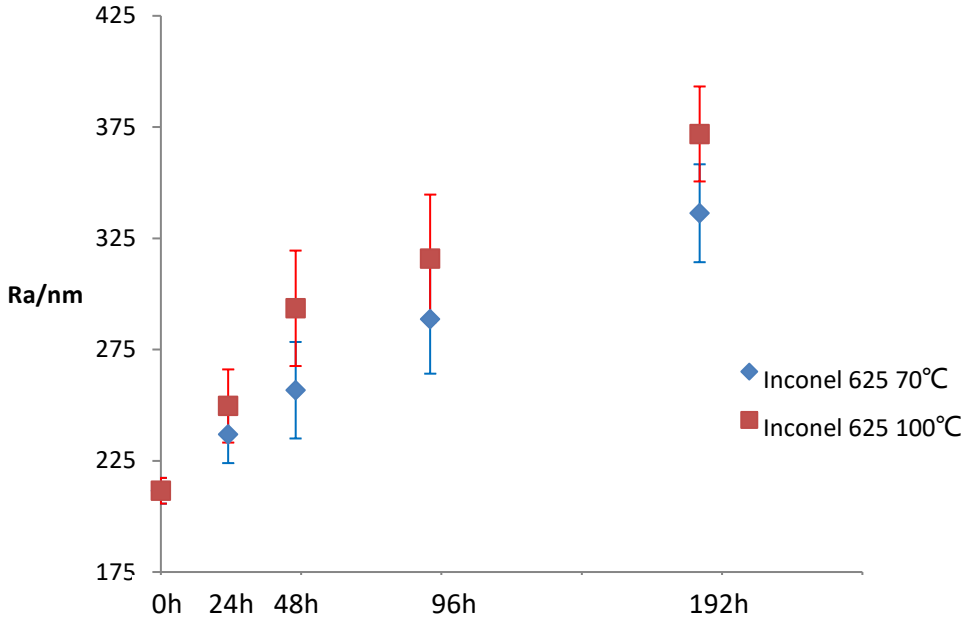

Figure 6 average roughness of Inconel 625

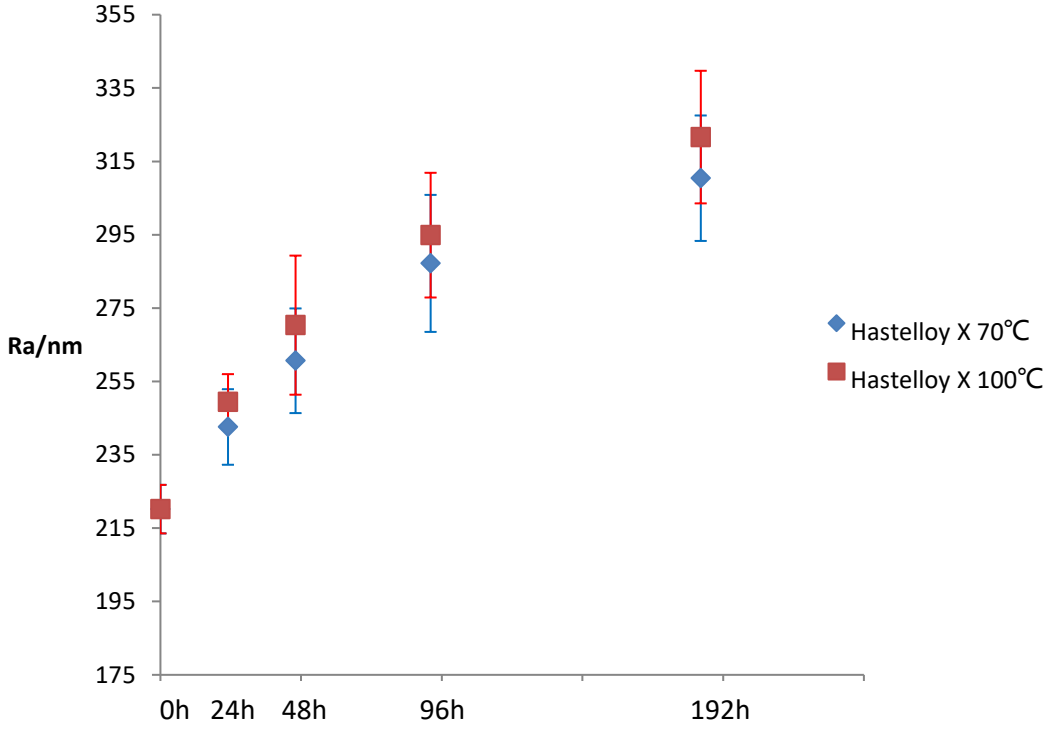

Figure 7 average roughness of Hastelloy X

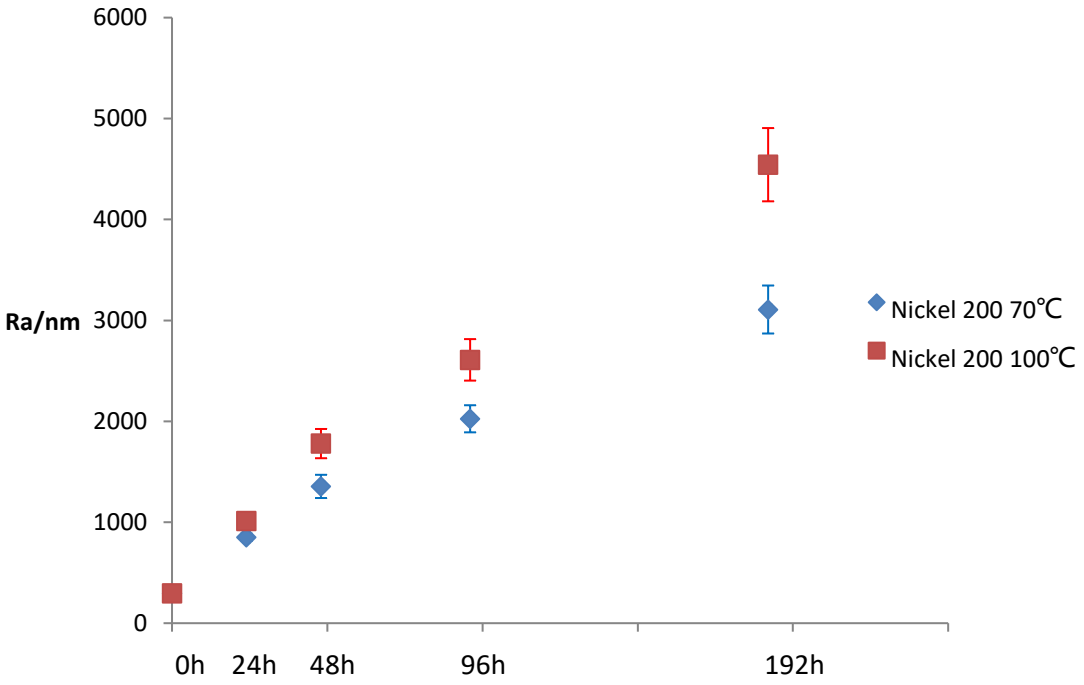

Figure 8 average roughness of Nickel 200

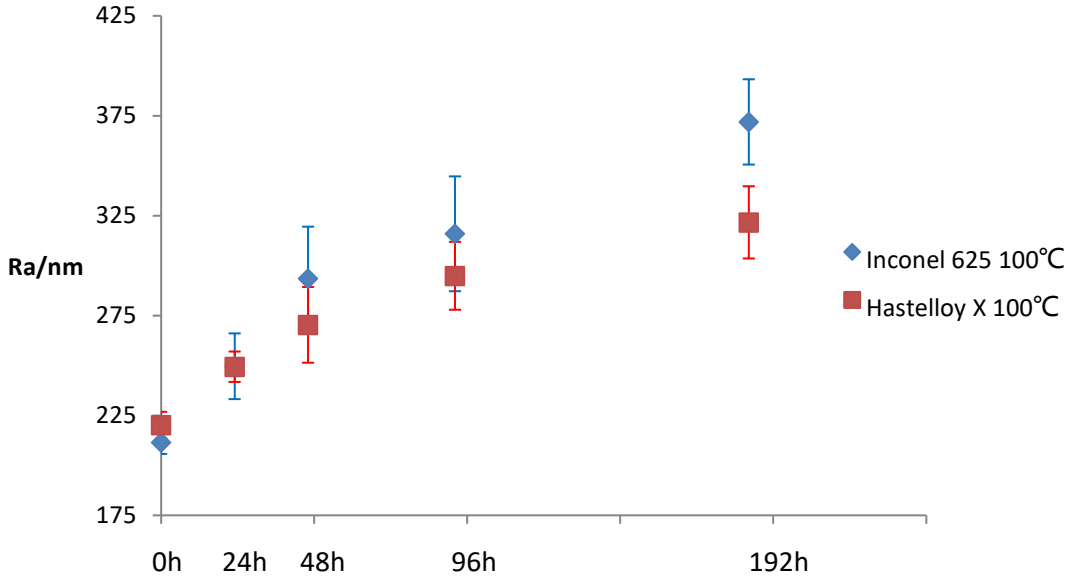

Figure 9 average roughness of Inconel 625 and Hastelloy X under 100℃

Fig.10 shows the morphology of nickel alloys before and after corrosion. After 96-hour corrosion in HI solution, the surface of Hastelloy X sample shows cracks, while Inconel 625 sample displays lots of small dents. Cracks and dents increase the roughness

of the samples to some extent. Both of these alloy specimens maintain relatively smooth surfaces after corrosion, while the Nickel 200 specimen has a rough surface, which indicates that the Nickel 200 alloy sample suffers more severe corrosion.

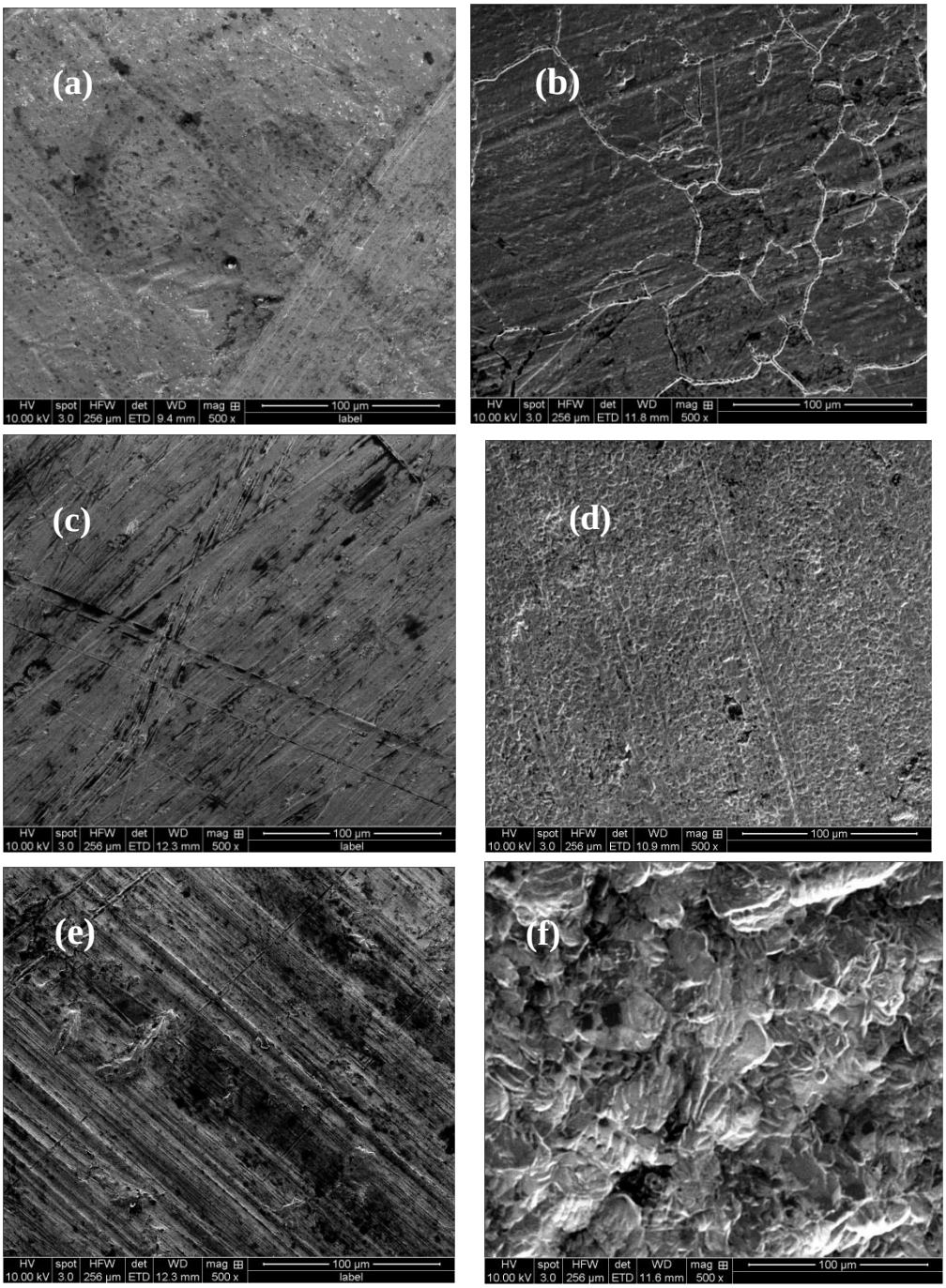

Figure 10 Comparison of original samples and after 70℃corrosion samples(a)original Hastelloy X (b) Hastelloy X after 96 hour corrosion(c)original Inconel 625 (d)Inconel after 96 hour corrosion (e)original Nickel 200(f) Nickel 200 after 96 hour corrosion

Fig 11 shows the effect of temperature on the morphology of nickel alloy. When temperature increases, the surface of Hastelloy X appears to show small dents as well as cracks. In terms of Inconel 625, when temperature goes to 100℃, the surface has many more dents. Both comparisons indicate that the higher temperature leads to more severe corrosion. There is no obvious difference in the morphology between Nickel 200 alloy samples at the two different temperatures. According to aforementioned weight loss and surface measurement experiments, the effect of temperature of morphology of Nickel 200 does exist, but is not readily apparent in the images.

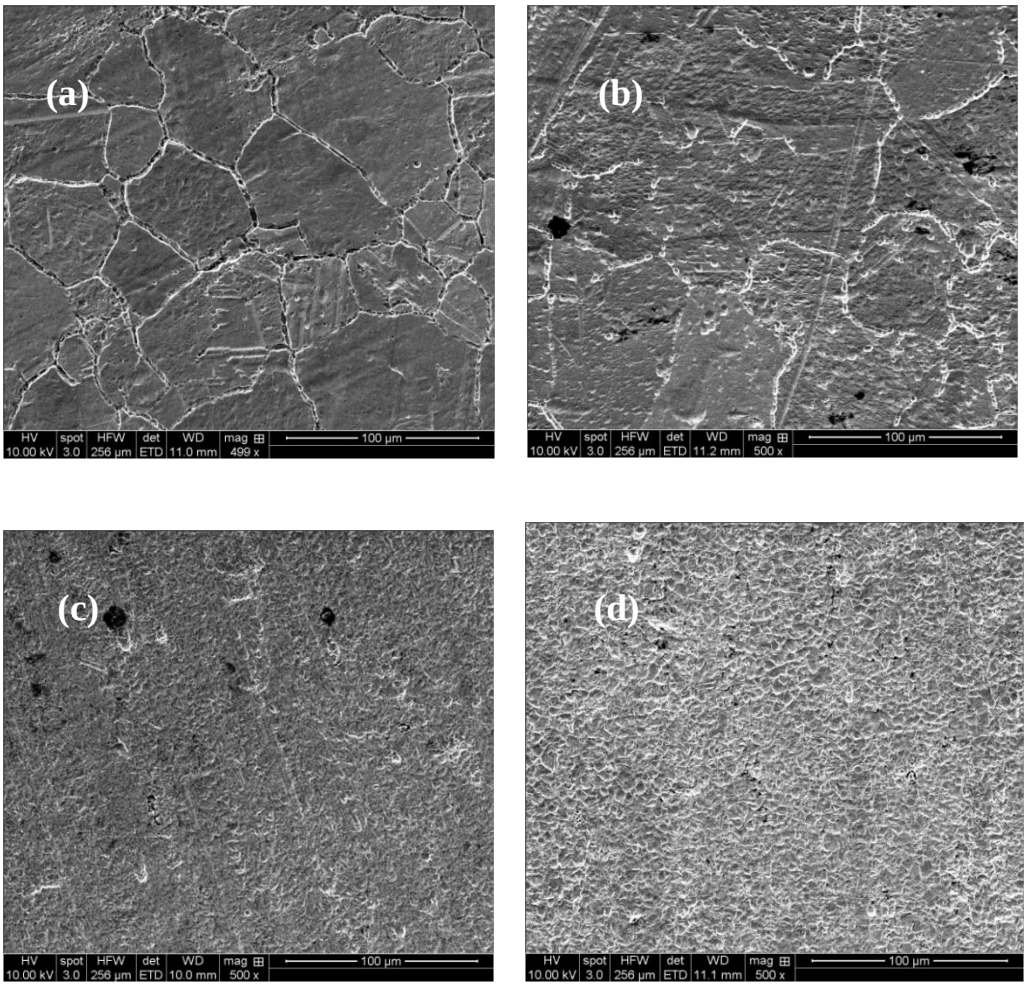

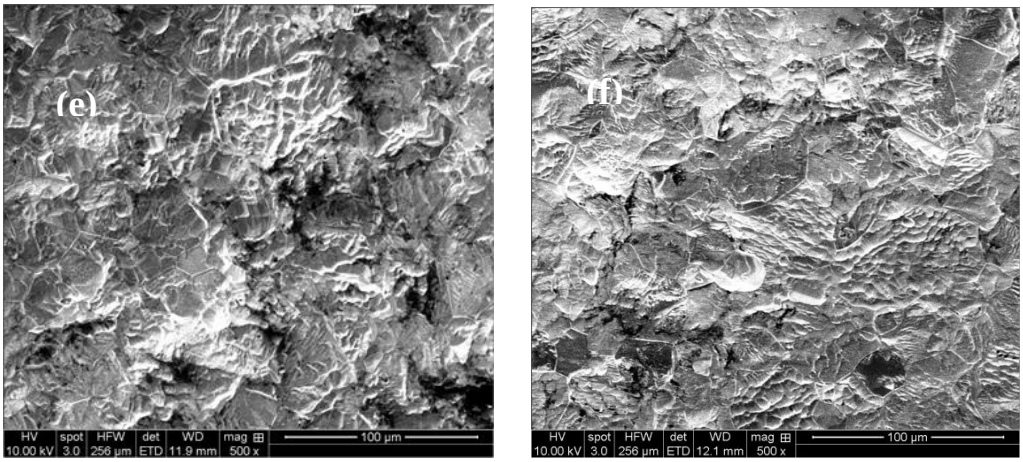

Figure 11 Effect of temperature on corrosion(a) Hastelloy X after 192 hour corrosion under 70℃(b) Hastelloy X after 192 hour corrosion under 100℃(c)7Inconel 625 after 192 hour corrosion under 70℃ (d)Inconel after 192 hour corrosion under 100℃ (e)7Nickel 200 after 192 hour corrosion under 70℃(f) Nickel 200 after 192 hour corrosion under 100℃

3.3 EDS Analysis

EDS can detect surface composition of alloy samples. Since nickel is the balance (base) element, the ratio of other element composition to nickel could reflect the changes of elemental composition with respect to nickel. The coefficients of variation of the ratios at different times are analyzed to indicate which element is relatively stable with respect to nickel in the corrosion.

$$\text{Coefficients of variation} = \frac{standard\ \ deviation\ \ of\ \ ratio}{average\ \ ratio}$$

In Inconel 625 samples, the Fe is quite stable compared with the other component elements according to Fig 12. In Hastelloy X, the Fe, Cr and Mo are each stable compared with its other constituent elements according to Fig 13. Since nickel is the base element of the alloy, the other elements which maintain a stable ratio to nickel, are corroding at a constant rate in the HI solution, with respect to nickel corrosion rate. In

Nickel 200 alloy, the composition of Nickel is quite high, so the composition of the other trace elements is too low to measure. The variations of ratio for each element with respect to nickel in this case are not as reasonable as the other two alloys. It is concluded that nickel is mainly the only constituent corroded in Nickel 200 alloy.

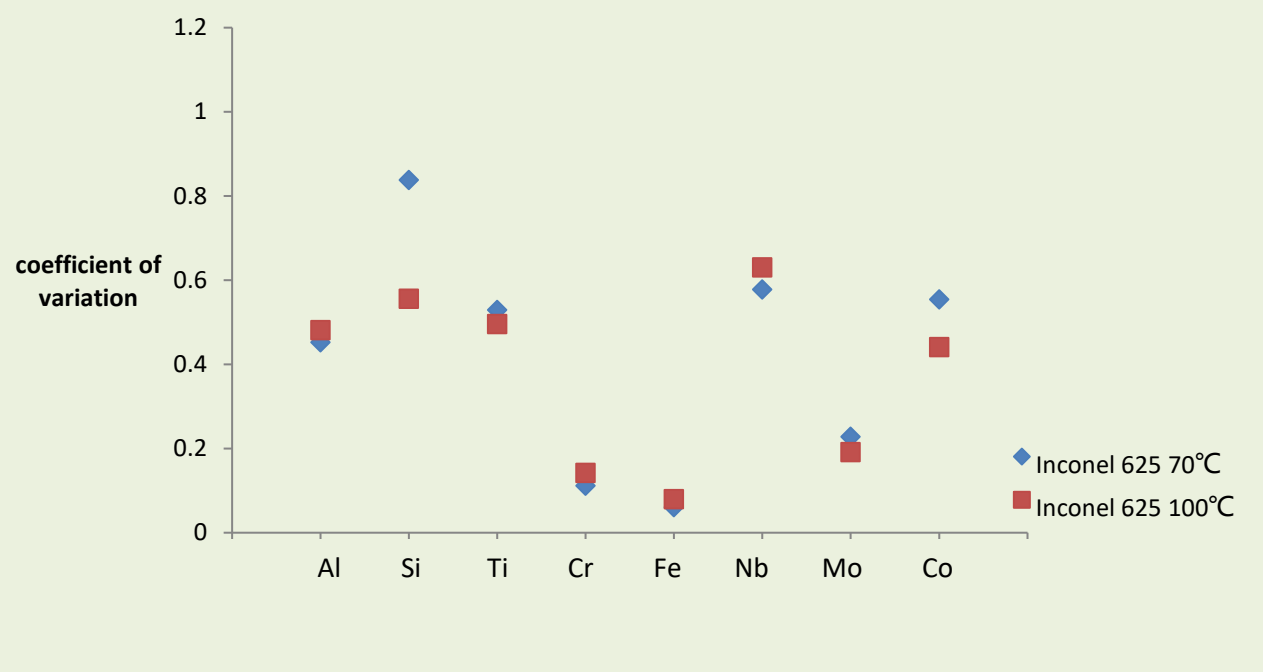

Figure 12 Coefficient of variation of each element with respect to Nickel of Inconel 625

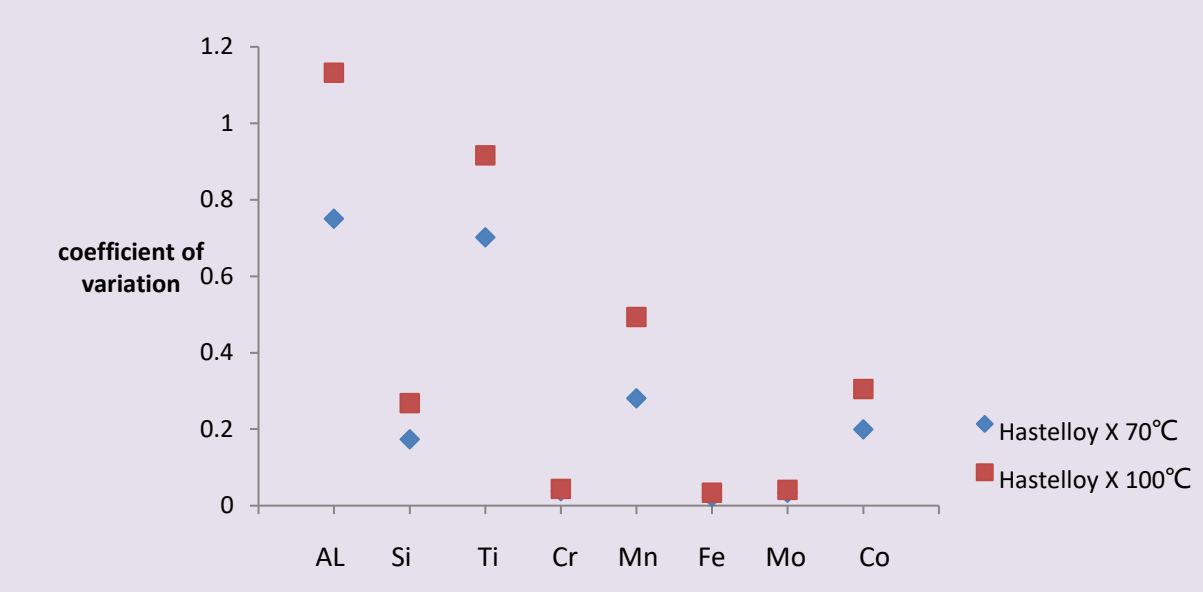

Figure 13 Coefficient of variation of each element with respect to Nickel of Hastelloy X

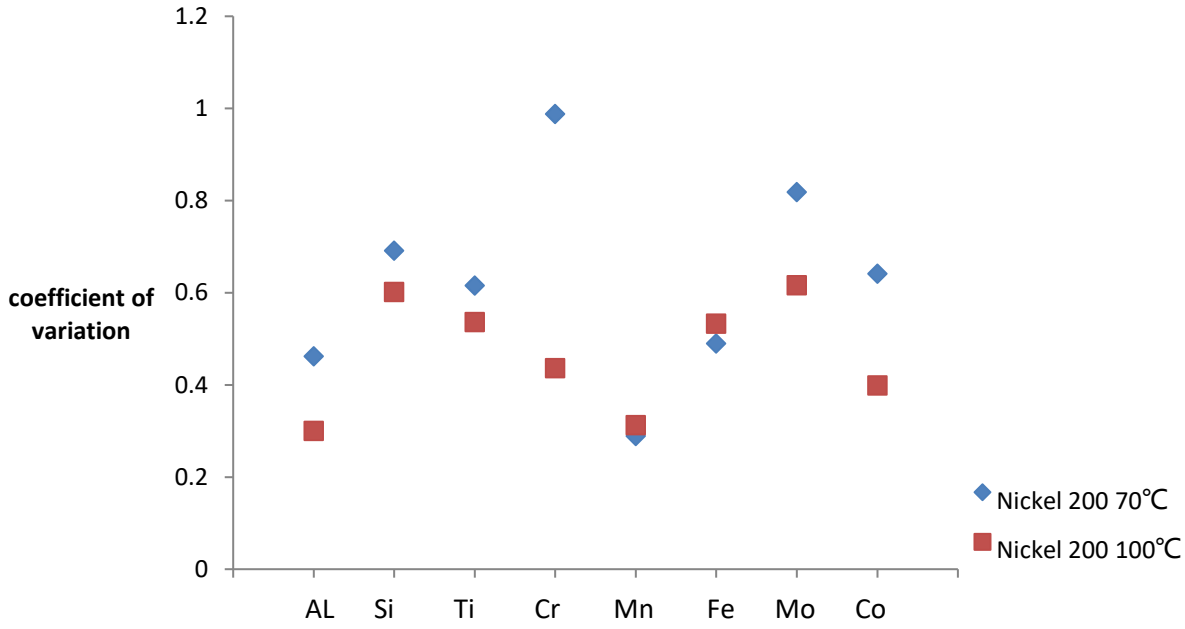

Figure 14 Coefficient of variation of each element with respect to Nickel of Nickel 200 alloy

The effect of temperature on the mass loss rate of elements is shown in Fig 15, Fig 16, Fig 17, and Fig 18. In Fig15, when temperature increases, the ratio of iron to nickel decreases, indicating the mass loss rate of iron increases with respect to nickel in Inconel

625. In Hastelloy X, the mass loss rate of iron, chromium and molybdenum increase as the temperature increases.

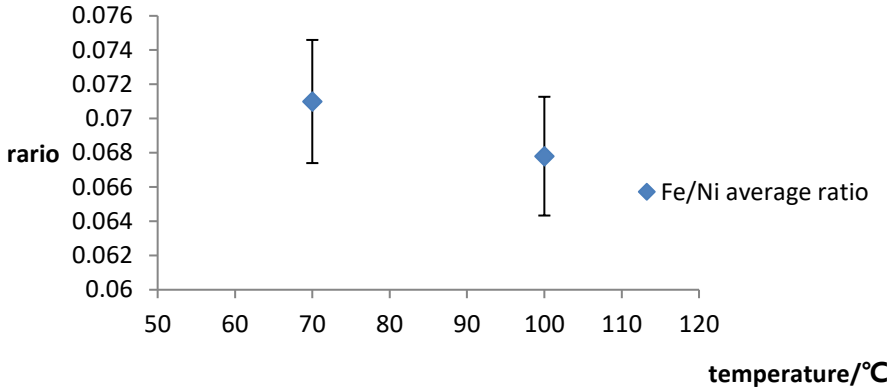

Figure 15 Fe/Ni average ratio in Inconel 625

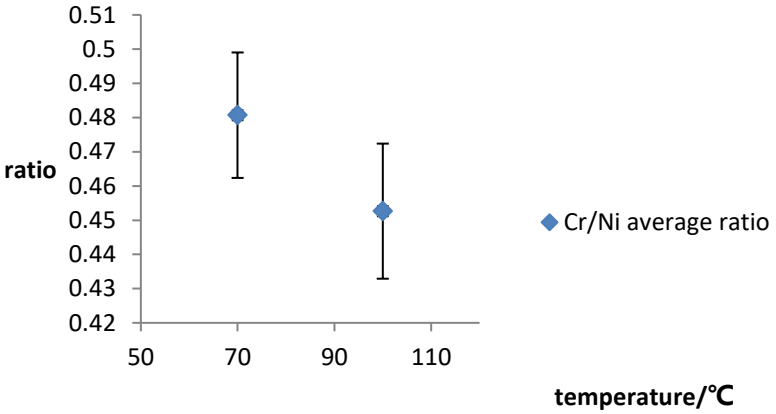

Figure 16 Cr/Ni average ratio in Hastelloy X

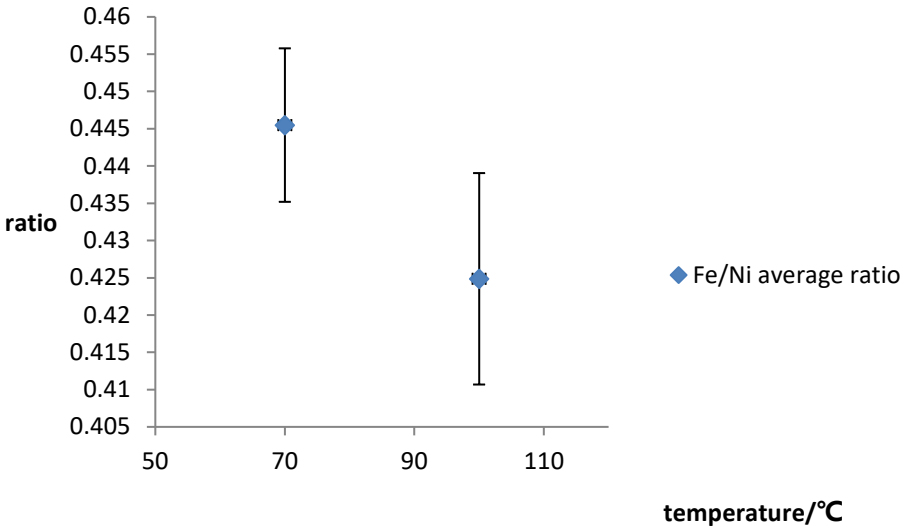

Figure 17 Fe/Ni average ratio in Hastelloy X

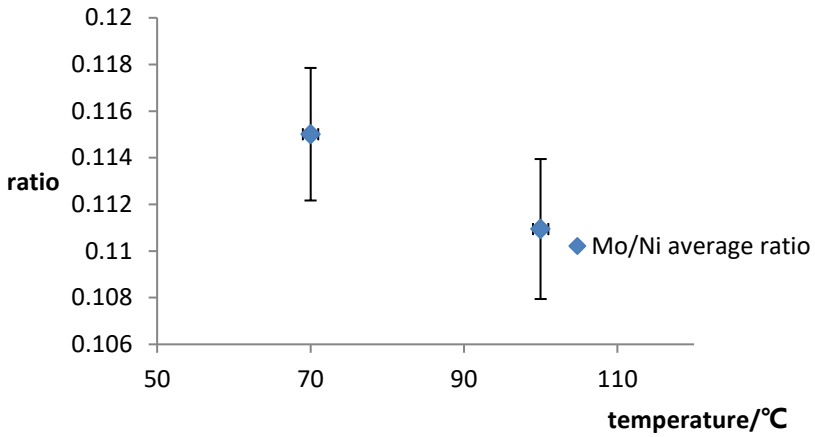

Figure 18 Mo/Ni average ratio in Hastelloy X

3.4 Pitting potential and Repassivation Potential

Pitting potential is the least positive potential at which pits can form. It is the potential at which the aggressive ion in solution is initiates breakdown of the passive metal oxide at the specimen's surface(Brookins 2012). The more positive the critical pitting potential, the more resistant the alloy is toward pit initiation.(Barbosa 2013).

Pitting potential is determined at the inflection above the sharp change in slope. Repassivation potentials can be determined as a cross-over potential on the return sweep in cyclic voltammetry. This potential is measured where the hysteresis loop closes.(Trueba and Trasatti 2015)

Temperature correlation of Ag/AgCl electrode:

t ℃ electrode potential(Zeng, Tang et al. 2014):

$$E_t = 0.2223 - 6 * 10^{-4} (t - 25)$$

When t = 70 ℃, the electrode potential is 192.3mV, and when t = 100, the electrode potential is 177.3mV. Fig 19, Fig 20, and Fig 21 show the pitting potential and repassivation potential of alloy samples with respect to SHE. The pitting potentials and repassivation potentials of all alloy samples are high, indicating a protective oxide layer. After 24 hour corrosion, both potentials decrease, which means the protective layers are damaged. After 48 hours corrosion, the pitting potentials and repassivation potentials of Hastelloy X and Inconel 625 increase again, while the potentials of Nickel 200 samples decrease very slightly. The oxide layer of Nickel 200 is damaged in the first 24 hour, while the oxide layer of the other two alloys insist to the second day.

At first, the pitting potential of Hastelloy X is larger than Inconel 625 because of a more resistant oxide layer, and then the pitting potential of Hastelloy X is slightly smaller than Inconel 625 in my results which may indicate that internal composition of Hastelloy X is not as resistant to corrosion as Inconel 625.

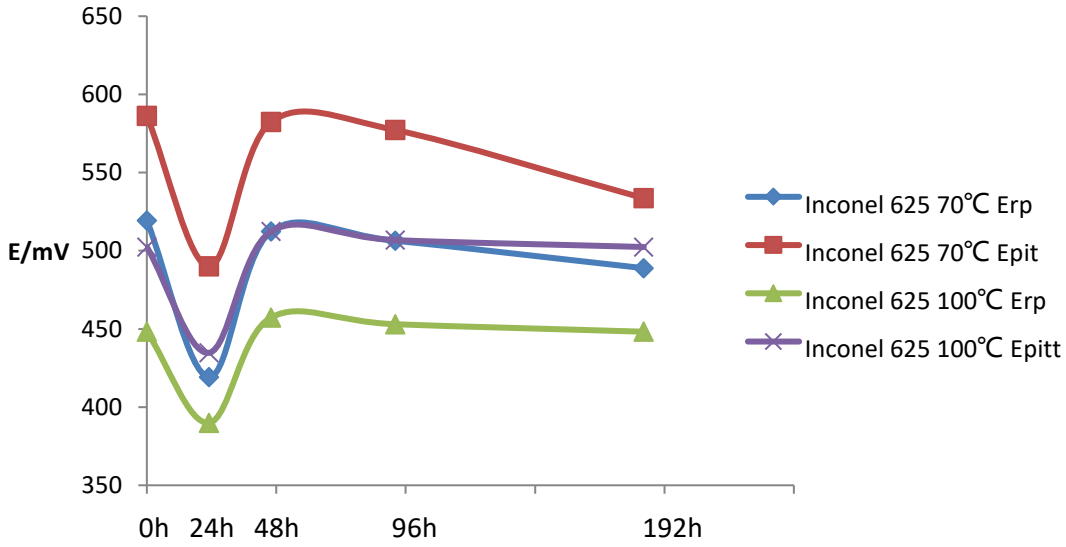

Figure 19 pitting potential and repassivation potential with respect to SHE of Inconel 625

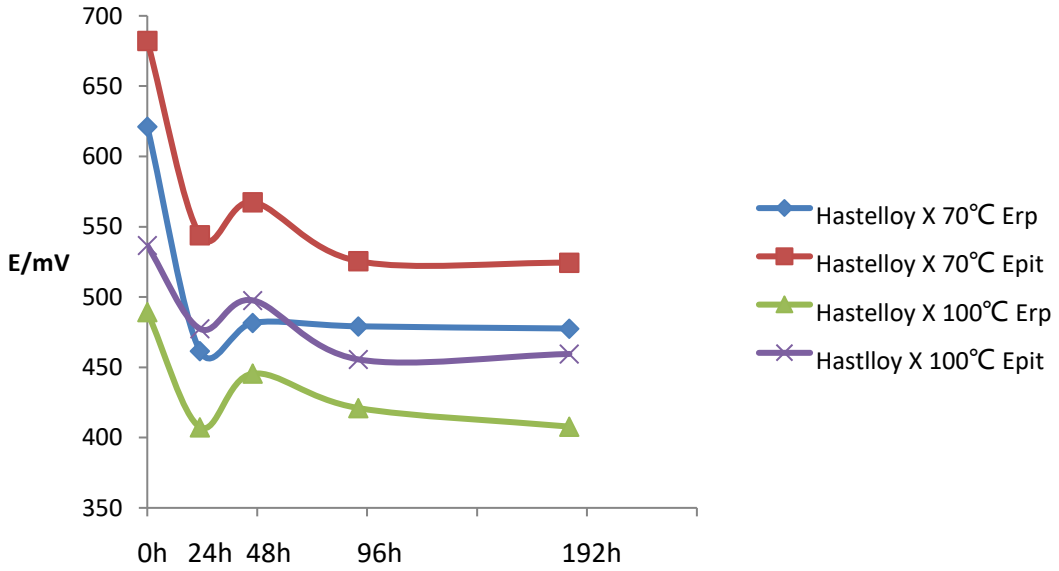

Figure 20 pitting potential and repassivation potential with respect to SHE of Hastelloy X

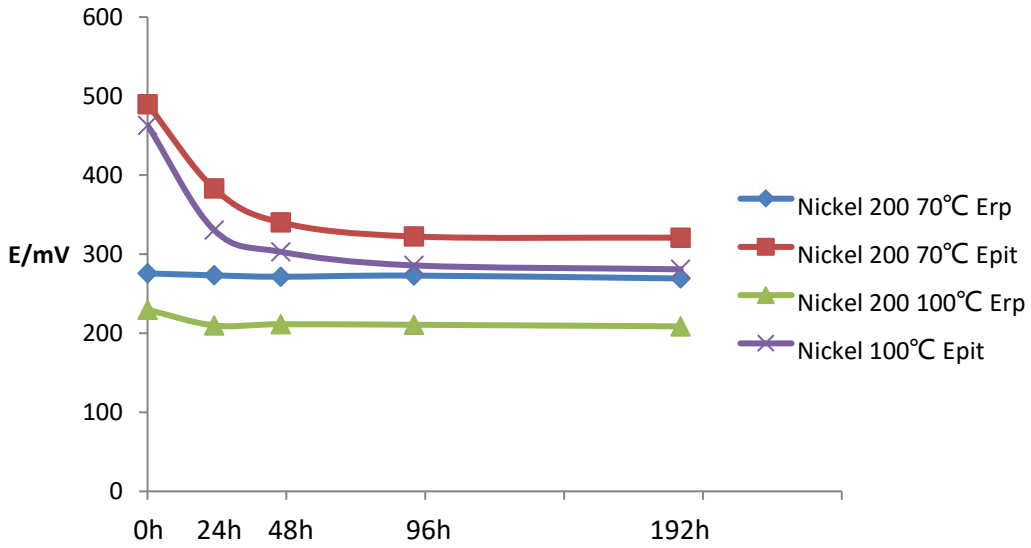

Figure 21pitting potential and repassivation potential with respect to SHE of Nickel 200

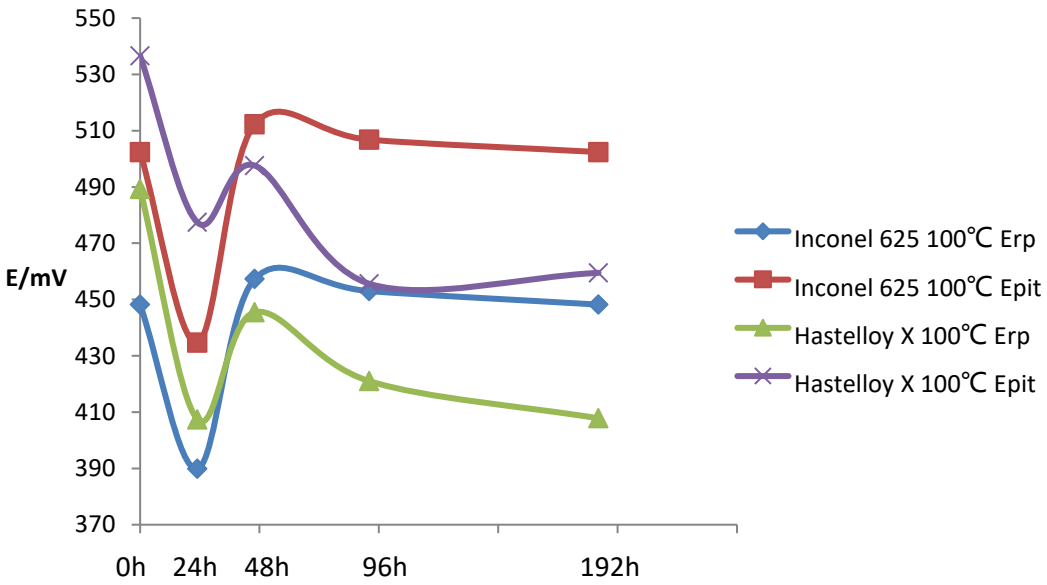

Figure 22 pitting potential and repassivation potential with respect to SHE of Inconel 625 and Hastelloy X under 100℃ corrosion

3.4 EIS analysis

The electrochemical impedance data for the nickel alloy samples after corrosion are shown in Fig 23 and Fig 24. The Nyquist plot shows that in terms of Inconel 625 and

Hastelloy X, the impedance decreases in the first 24 hours, and then increases. The impedances of 48 hour, 96 hour, and 192 hour have no significant differences.

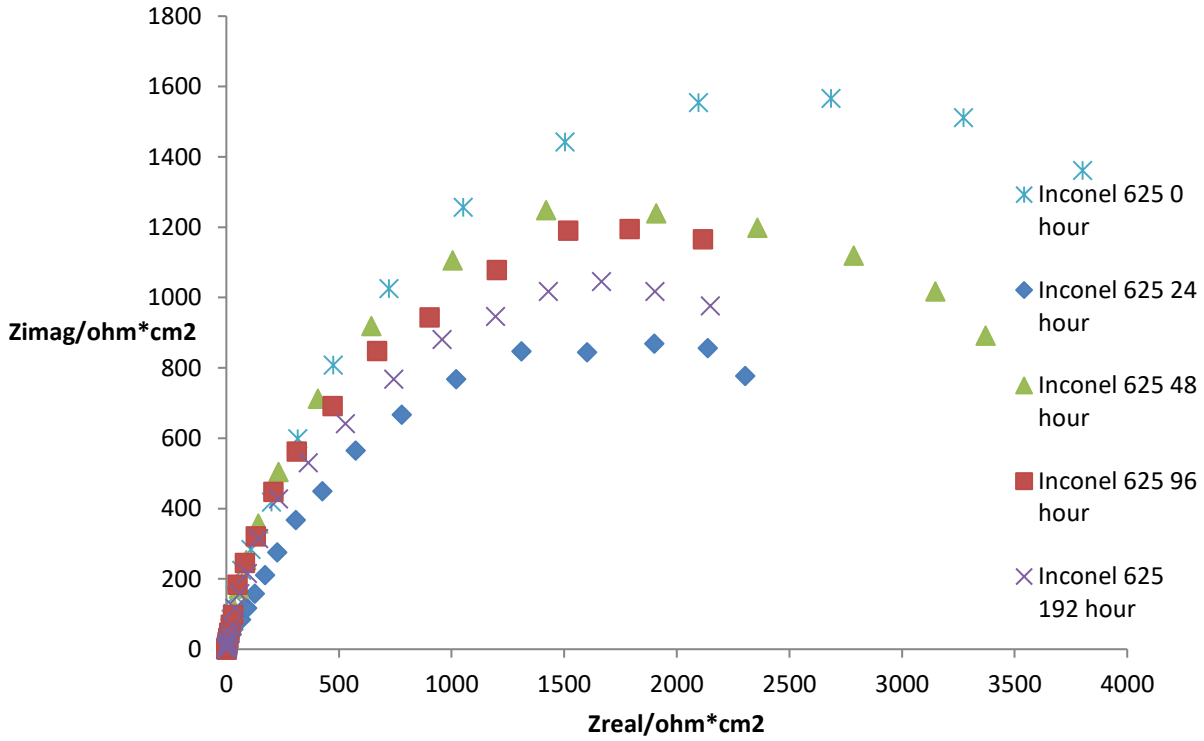

Figure 23 Nyquist plot of Inconel 625 in HI solution under 70℃

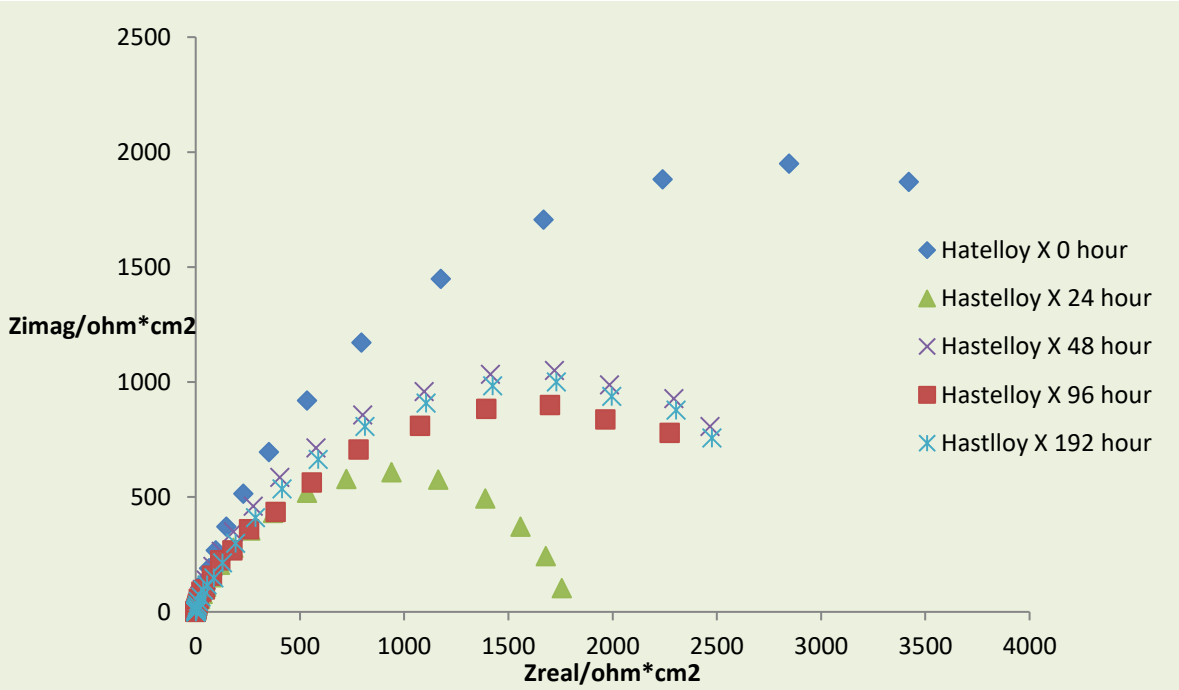

Figure 24 Nyquist plot of Hastelloy in HI solution under 70℃

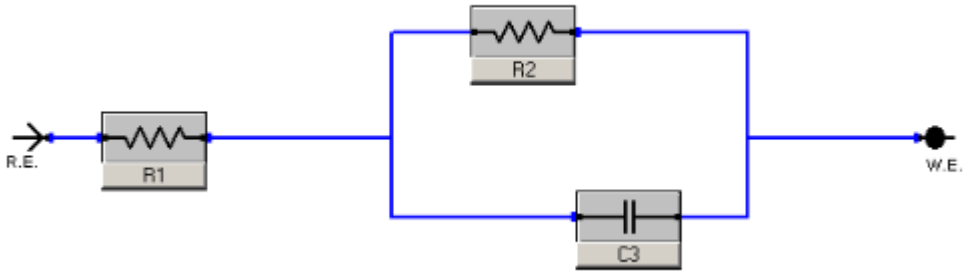

Figure 25 the equivalent circuit to fit the EIS for nickel alloy corrosion. R1, resistance of electrolyte solution. R2, charge transfer resistance. C3, capacitance of double layer between the surface of alloy and electrolyte.

The impedance spectrum of the nickel alloys is fitted by the equivalent circuit model displayed in Fig 25. R1 represents the resistance of the electrolyte solution, R2 represents the charge transfer resistance, and C3 represents the capacitance of double layer between the surface of alloy and electrolyte. When fitting the equivalent circuit model to EIS data, Gamry utilizes a downhill simplex method to optimize the fit parameter(Qiu, Tang et al. 2013). The simplex method was first described by Nelder and Mead.(Nelder 1965/01/01)

They described the simplex method as a method which adapts itself to the local landscape and contracts to a final minimum. The advantage is that it does not require derivatives, just function evaluations. The goodness of fit is determined by the Chi squared method. Chi squared is the calculated sum of the weighted residuals, defined as follows:

$$\chi^2 = \sum_{i=1}^{N} w_i \left[(Zmeas_{real} - Zfit_{real})^2 + (Zmeas_{imag} - Zfit_{imag})^2 \right]$$

Weighting is calculated as follows based on user input:

Zmod weighting:

$$w_i = \frac{1}{\sqrt{(Zmeas_{i,real}{}^2 + Zmeas_{i,imag}{}^2}}$$

Errors are calculated using Maximum Likelihood Estimation.

The fitting result is shown in Table 2. The resistances of solution have no significant differences. The capacitances of double layer have an increasing tendency because of the increasing roughness of the sample surface. Fig 26 and Fig 27 show the tendency of charge transfer resistance. The smaller charge transfer resistance, the faster the corrosion reaction rate.

Table 2 EIS Data Fitting Using the Equivalent Circuit model

70℃	R1/ohm*cm2	error/ohm*cm2	R2/ohm*cm2	error/ohm*cm2	C3/uF	error/uF	goodness of fit/10-3
Inconel625							
0	1.519	0.005032	2811	7.547	5.97	0.0162	120.8
24	1.337	0.01325	1428	7.496	6.716	0.0122	177.4
48	1.443	0.004459	1911	5.326	7.711	0.01109	97.85
96	1.56	0.004661	1766	2.764	8.958	0.0138	150.5
192	1.261	0.008539	1717	6.132	9.233	0.01474	191.5
Hastelloy X							
0	1.224	0.004837	3019	4.052	11.79	0.03724	141.7
24	1.301	0.009318	1267	4.207	12.47	0.02341	189.8
48	1.205	0.003688	1612	3.077	12.63	0.01961	171.2
96	1.313	0.004745	1555	2.16	12.99	0.009339	138.9
192	1.359	0.04026	1432	3.7979	13.55	0.03572	75.18
Nickel 200							
0	1.455	0.003806	1455	2.659	7.76	0.02066	77.36
24	1.058	0.004742	626	1.837	7.58	0.01021	154.1
48	1.271	0.00566	503	1.977	8.466	0.008712	177.3
96	1.503	0.006937	484	1.794	9.933	0.01755	191.9
192	1.295	0.002271	308	1.017	10.7	0.01926	147.1

100℃	R1/ohm*cm2	error/ohm*cm2	R2/ohm*cm2	error/ohm*cm2	C3/μF	error μF	goodness of fit/10-3
Inconel625							
0	1.234	0.01094	362.5	2.053	10.5	0.04167	164.2
24	1.009	0.01853	196.1	1.624	12.673	0.01921	49.64
48	1.153	0.003512	305.4	0.596	12.813	0.05032	203.6
96	1.243	0.002564	292.49	0.06563	13.202	0.0114	46.79
192	0.996	0.004838	283.04	0.1148	13.967	0.008376	64.87
Hastelloy X							
0	0.849	0.001704	445	0.2965	15.95	0.02628	129.7
24	0.808	0.002405	177.1	0.8909	17.32	0.05566	193.1
48	1.451	0.007341	273.4	0.1424	18.867	0.006713	109.6
96	1.166	0.00457	244.45	0.726	18.665	0.01573	209.2
192	1.422	0.002878	244.12	0.9194	18.3	0.02664	205.7
Nickel 200							
0	1.205	0.003481	289.1	0.1097	10.12	0.02613	75.23
24	1.245	0.005232	234.3	0.3452	10.58	0.02376	103.2
48	1.686	0.005432	64.29	0.5886	12.18	0.01822	146.6
96	1.16	0.003212	55.68	0.1096	11.79	0.04494	119.5
192	1.105	0.00244	43.47	0.1489	14.82	0.0179	120.66

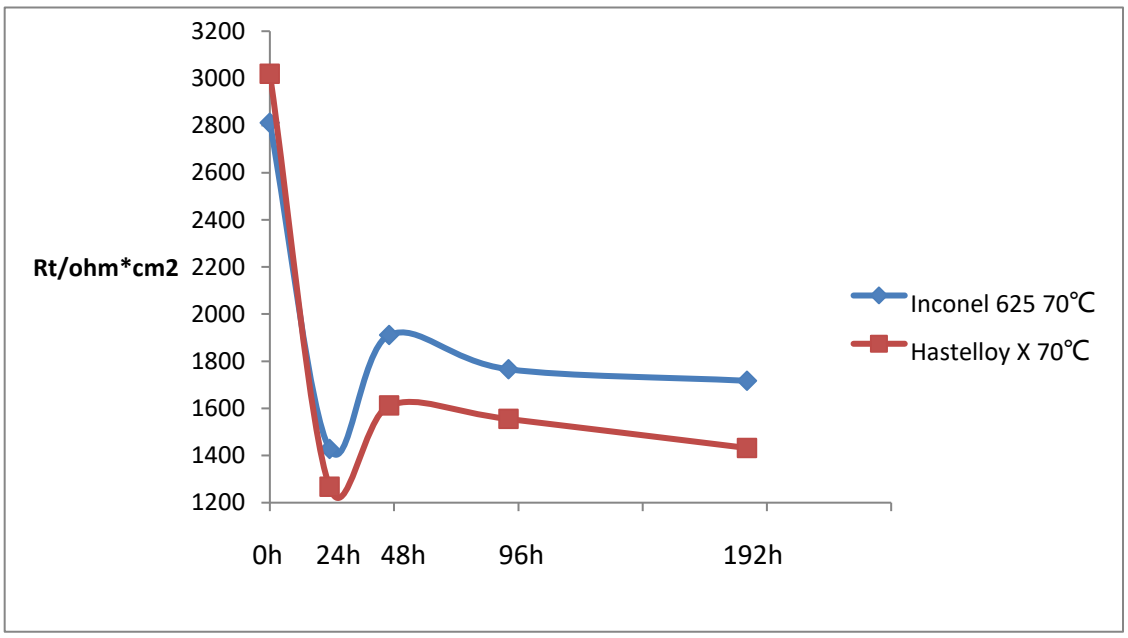

Figure 26 charge transfer resistance change of Inconel 625 and Hastelloy X in 70℃

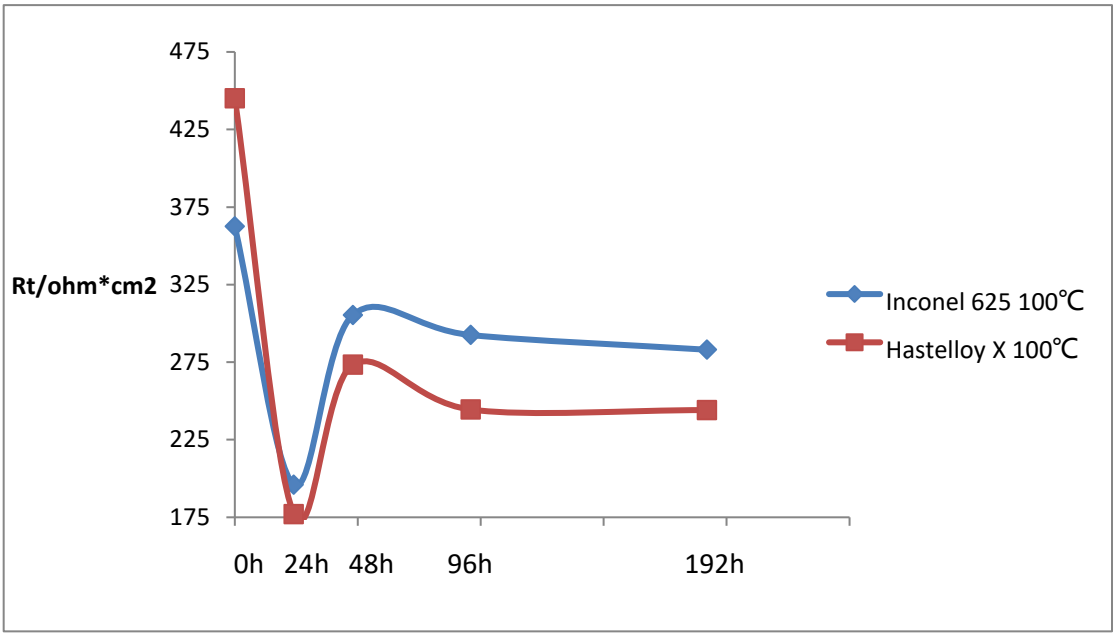

Figure 27 charge transfer resistance change of Inconel 625 and Hastelloy X in 100℃

CHAPTER 4

Conclusions and Future Work

4.1 Conclusion

In this work, the corrosion performance of three Ni-based alloys in HI solution is analyzed by weight loss measurement, optimal profiler roughness measurement, SEM, and electrochemical methods. The corrosion rates of all alloys increase with temperature goes up. In terms of Inconel 625 and Hastelloy X, the corrosion rate increases and then goes down to a flat tendency as time intervals increase. This phenomenon is considered because of their anti-corrosion layer. While in Nickel 200, the corrosion rate does not fluctuate remarkably, since the protective layer is weaker than the other two. In Inconel 625 samples, the iron is lost in a stable ratio of rate with respect to nickel. While in Hastelloy X samples, the iron, Chromium, and Molybdenum are corroded in a constant ratio of rates with respect to nickel, respectively. With temperature increases, the ratio of these elements to nickel decreases, which means the corrosion rates of these element increase.

4.2 Future work

In order to continue exploring the internal mechanism more deeply, other experimental method could be considered, like X-ray diffraction(Ko, Ingham et al. 2014).

Second, the corrosion performance of Nickel alloy in HI gas phase flow should also be conducted, the corrosion temperature also need to be increased, to simulate the industrial environment, so that a more reasonable choice could be made for future hydrogen.(Ramos-Sanchez, Jeans et al. 2015)

References

Barbosa, M. A. M. d. R. (2013). "Passivation kinetics and pitting studies on Cr, Ni and an 18Cr-10Ni stainless steel."

Brookins, D. G. (2012). Eh-pH diagrams for geochemistry, Springer Science & Business Media.

Brown, C., et al. (2013). "Effects of microstructure on long and short crack growth in nickel base superalloys." Metal science.Choi, J. Y., et al. (2014). "Corrosion resistances of alloys in high temperature hydrogen iodide gas environment for sulfur–iodine thermochemical cycle." International Journal of Hydrogen Energy **39**: 14557-14564.

Fu, G., et al. (2016). "Effect of raw material sources on activated carbon catalytic activity for HI decomposition in the sulfur-iodine thermochemical cycle for hydrogen production." International Journal of Hydrogen Energy **41**: 7854-7860.

Goldstein, J., et al. (2012). Scanning electron microscopy and X-ray microanalysis: a text for biologists, materials scientists, and geologists, Springer Science & Business Media.

Gorensek, M. (2010). The Sulfur-Iodine Cycle: Process Analysis and Design Using Comprehensive Phase Equilibrium Measurements and Modeling.

Iden, H. and A. R. Kucernak (2014). "Analysis of effective surface area for electrochemical reaction derived from mass transport property." Journal of Electroanalytical Chemistry **734**: 61-69.

Jomard, F., et al. (2008). "Numerical modeling for preliminary design of the hydrogen production electrolyzer in the Westinghouse hybrid cycle." International Journal of Hydrogen Energy **33**(4): 1142-1152.

Ko, M., et al. (2014). "In situ synchrotron X-ray diffraction study of the effect of chromium additions to the steel and solution on CO 2 corrosion of pipeline steels." Corrosion Science **80**: 237-246.

Lee, M. S., et al. (2009, 1/1/2009). "Immobilization of calcium oxide solid reactant on a yttria fabric and thermodynamic analysis of UT-3 thermochemical hydrogen production cycle." International Journal of Hydrogen Energy.

Liu, M., et al. (2013). "Investigation on corrosion behavior of Ni-based alloys in molten fluoride salt using synchrotron radiation techniques." Journal of Nuclear Materials **440**: 124-128.

Mishra, A. and D. Shoesmith (2015). Effect of Copper on Crevice Corrosion Inhibition of Nickel-Chromium-Molybdenum Alloy in Aggressive Conditions. CORROSION 2015, NACE International.

Murphy, J. E. and J. P. O'Connell (2012). "Process simulations of HI decomposition via reactive distillation in the sulfur–iodine cycle for hydrogen manufacture." International Journal of Hydrogen Energy **37**(5): 4002-4011.

Nelder, J. A. M., R. (1965/01/01). "A Simplex Method for Function Minimization." The Computer Journal **7**(4).

Nguyen, T. D. B., et al. (2014). "Kinetics and modeling of hydrogen iodide decomposition for a bench-scale sulfur–iodine cycle." Applied Energy **115**: 531-539.

Poza, P., et al. (2014). "Mechanical properties of Inconel 625 cold-sprayed coatings after laser remelting. Depth sensing indentation analysis." Surface and Coatings Technology **243**: 51-57.

Qiu, J., et al. (2013). "XPS and electrochemical impedance spectroscopy studies on effects of the porcelain firing process on surface and corrosion properties of two nickel–chromium dental alloys." Journal of Materials Science: Materials in Medicine **24**(11): 2519-2528.

Ramos-Sanchez, V., et al. (2015). "A unique approach to the vapour phase of the HI x feed of the sulfur iodine thermochemical cycle: A Raman spectroscopy study." International Journal of Hydrogen Energy **40**(4): 1657-1664.

Ross, R. B. (2013). Metallic materials specification handbook, Springer Science & Business Media.

Sitek, R., et al. (2012). "Microstructure and properties of ultrafine grain nickel 200 after hydrostatic extrusion processes." Materials Science-Poland **30**(3): 282-289.

Trueba, M. and S. P. Trasatti (2015). "Electrochemical approach to repassivation kinetics of Al alloys: gaining insight into environmentally assisted cracking." Corrosion Reviews **33**(6): 373-393.

Vetter, K. J. (2013). Electrochemical kinetics: theoretical aspects, Elsevier.

Vitart, X., et al. (2006). "Hydrogen production using the sulfur ‑ iodine cycle coupled to a VHTR: an overview." Energy conversion and management **47**(17): 2740-2747.

Wang, F. (2012). "Mechanical property study on rapid additive layer manufacture Hastelloy® X alloy by selective laser melting technology." The International Journal of Advanced Manufacturing Technology **58**(5-8): 545-551.

Ying, Z., et al. (2013). "Electrochemical investigation of the Bunsen reaction in the sulfur–iodine cycle." International Journal of Hydrogen Energy **38**(34): 14391-14401.

Zeng, L., et al. (2014). "A high-performance alkaline exchange membrane direct formate fuel cell." Applied Energy **115**: 405-410.